Two-dimensional fluctuating vesicles in linear shear flow

R. Finken, A. Lamura, U. Seifert and G. Gompper

Two-dimensional fluctuating vesicles in linear shear flow

R. Finken[1,a], A. Lamura[2,b], U. Seifert[1,c], and G. Gompper[3,d]

[1] II. Institut für Theoretische Physik, Universität Stuttgart, 70550 Stuttgart, Germany
[2] Istituto Applicazioni Calcolo, Consiglio Nazionale delle Ricerche (CNR), Via Amendola 122/D, 70126 Bari, Italy
[3] Forschungszentrum Jülich GmbH, Institut für Festkörperforschung, 52425 Jülich, Germany

Abstract. The stochastic motion of a two-dimensional vesicle in linear shear flow is studied at finite temperature. In the limit of small deformations from a circle, Langevin-type equations of motion are derived, which are highly nonlinear due to the constraint of constant perimeter length. These equations are solved in the low-temperature limit and using a mean-field approach, in which the length constraint is satisfied only on average. The constraint imposes non-trivial correlations between the lowest deformation modes at low temperature. We also simulate a vesicle in a hydrodynamic solvent by using the multi-particle collision dynamics technique, both in the quasi-circular regime and for larger deformations, and compare the stationary deformation correlation functions and the time autocorrelation functions with theoretical predictions. Good agreement between theory and simulations is obtained.

PACS. 87.16.D- Membranes, bilayers, and vesicles – 87.15.Ya Fluctuations – 47.15.G- Low-Reynolds-number (creeping) flows

1 Introduction

The dynamics of soft objects such as drops, capsules and cells in flow represents a long-standing problem in science and engineering, but has received increasing interest recently, in particular due to its relevance to biological, medicinal and microfluidic applications. This problem is challenging from a theoretical point of view, because the shape of these objects is not given *a priori*, but determined dynamically from a balance of interfacial forces with fluid stresses. Improved experimental methods have revealed intriguing new dynamical shape transitions due to the presence of shear flow. The phenomenology of the dynamical behavior depends distinctively on the specific soft object immersed in the flow with fluid bilayer vesicles and elastic microcapsules as the most prominent classes.

Fluid bilayer vesicles assume a stationary tank-treading shape in linear shear flow, if there is no viscosity contrast between interior and exterior fluid [1]. If the interior fluid or the membrane becomes more viscous, a transition to a tumbling state can occur [2–7]. Tank-treading was observed experimentally in infinite shear flow [8, 9] and for vesicles interacting with a rigid wall [10,11],

where a dynamic lift occurs [12–15]. The tank-treading–to–tumbling transition was observed for the first time convincingly in experiment only very recently [16,17]. In addition to the tank-treading–to–tumbling transition, an oscillating motion was predicted theoretically [18] and observed experimentally [16] and in simulations [19]. This type of motion has alternatively been called vacillating-breathing [18], swinging [19], or trembling [16,20]. The theoretical description has been extended recently beyond first order in the shear rate [19–21].

At finite temperature, stochastic fluctuations of the membrane due to thermal motion affect the motion of the object. Due to the dissipative nature of the hydrodynamic interactions, vesicles in shear flow form a non-trivial model system for studying non-equilibrium stochastic dynamics. Since the effect of thermal noise on the transitions between the different modes of motion in general is a challenging task, in this paper we concentrate on the stochastic motion in the stationary tank-treading state. Our theoretical approach is similar to that of reference [22], where stochastic equations of motion were derived for quasi-spherical vesicles.

Most numerical methods solving the equation of motion of vesicles or capsules [1,2] operate in the absence of thermal forces. An exception, which naturally includes thermal noise, is multi-particle collision dynamics (MPC), also known as stochastic rotation dynamics (SRD) [23–26]. In this method, the fluid part is modeled on a particle

ᵃ e-mail: finken@theo2.physik.uni-stuttgart.de
ᵇ e-mail: a.lamura@ba.iac.cnr.it
ᶜ e-mail: useifert@theo2.physik.uni-stuttgart.de
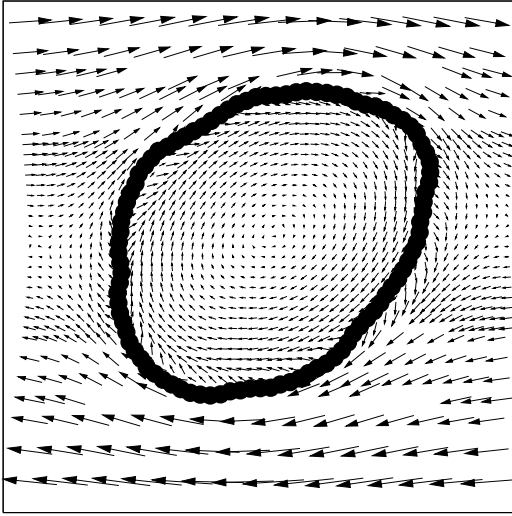ᵈ e-mail: g.gompper@fz-juelich.de

Fig. 1. Snapshot of the vesicle and the velocity field around it, taken from simulation data for reduced area $A^* = 0.95$ and reduced shear rate $\chi \simeq 5.6$ (see Eq. (28)). The disks represent the beads forming the membrane and are plotted to scale.

rather than a continuum level. The microscopic equations of motion for the effective fluid are chosen to be evaluated efficiently on the one hand, and on the other hand to lead to the correct macroscopic hydrodynamics. This method has successfully been applied to flow around rigid objects [27,28], polymers [29,30] and viscous vesicles [5,6, 31,19]. We employ the MPC simulation method to compare our theoretical predictions of correlation functions, inclination angles, and tank-treading frequencies with simulation data of vesicles. In order to obtain good statistics, we focus here on two-dimensional (2d) vesicles with a linear boundary.

The paper is organized as follows: After formulating the problem in Section 2, we outline the derivation of nonlinear stochastic equations of motion for quasi-circular vesicles in Section 3. These are solved approximately using a mean-field approach and a low-temperature expansion in Section 4. We also present the 2d version of the deterministic Keller-Skalak theory [32] in Section 5, which takes into account the influence of the vesicle shape on the flow. The simulation method used is discussed in Section 6. Finally we compare the calculations with simulation data in Section 7 and discuss our results. The detailed derivation of the equations of motion is given in the Appendix.

2 Problem formulation

We consider a model 2d vesicle immersed in a fluid of viscosity η_{out} with a 1d membrane boundary surrounding a fluid of viscosity η_{in} and at finite temperature T. A snapshot of a vesicle together with the fluid velocity field taken from simulation data (cf. Sect. 6) is shown in Figure 1. Due to the incompressibility of the membrane and of the enclosed fluid, the area A_0 and the length L_0 of the

membrane are constants. The membrane resists deformation with a bending rigidity κ, which is defined rigorously below in Section 2.1. The fixed area defines a length scale

$$R_0 \equiv \sqrt{\frac{A_0}{\pi}}, \tag{1}$$

which can be used to define a number of dimensionless quantities. In the following, we use the excess length

$$\Delta \equiv \frac{L_0}{R_0} - 2\pi \tag{2}$$

and the dimensionless viscosity contrast

$$\lambda \equiv \frac{\eta_{\mathrm{in}}}{\eta_{\mathrm{out}}}. \tag{3}$$

Alternatively one can derive a length $R^* \equiv L_0/(2\pi)$ from the length constraint, and use it to define a reduced area $A^* \equiv A_0/(\pi R^{*2})$. The reduced area is connected to the excess length by

$$A^* = \left(1 + \frac{\Delta}{2\pi}\right)^{-2}. \tag{4}$$

In a quiescent fluid, thermal stochastic forces acting on the membrane lead to a fluctuating shape, where the probability of any specific deformation can be calculated using the Boltzmann weight corresponding to the deformation energy $\mathcal{H}[\mathbf{r}]$. If an external flow field $\mathbf{v}^\infty$ is switched on, the system ceases to be in equilibrium, and the statistical weight of a deformation cannot be calculated *a priory* using Boltzmann weights. We first derive the force balance governing the motion of a vesicle in Stokes flow, before we simplify the equations of motion in the limit of small deformations from a circular shape. Thermal noise is added by assuming equilibrium statistics.

2.1 Constitutive equation of the membrane

We employ conventions of differential geometry following reference [33]. The shape of the vesicle is given by the shape function $\mathbf{r}(s)$, where $0 \leq s \leq L$ denotes the arc length. The tangent vector $\mathbf{t}(s) \equiv \mathrm{d}\mathbf{r}(s)/\mathrm{d}s$ is of unit length. The unit normal vector $\mathbf{n}(s)$ is defined to point to the outside of the vesicle, and the orientation is chosen such that the pair $(\mathbf{n}, \mathbf{t})$ forms a right-handed system. The curvature $k(s)$ is defined via the relation

$$\mathrm{d}\mathbf{t}(s)/\mathrm{d}s = -k(s)\mathbf{n}(s). \tag{5}$$

The 2d analog of the bending energy of a certain membrane deformation is given by the Helfrich term [34]

$$\mathcal{H}_\kappa[\mathbf{r}] \equiv \frac{\kappa}{2} \int_0^L \mathrm{d}s \, k(s)^2, \tag{6}$$

which corresponds also to the bending energy of a semi-flexible polymer [35]. Note that for 3d vesicles, a spontaneous curvature C_0 can appear in the bending energy for

intrinsically asymmetric monolayers or asymmetric liquid environments. In 2d vesicles, we can ignore the spontaneous curvature, since it shifts the bending energy only by a topological constant, much like the Gaussian curvature contribution to the curvature energy can be ignored in 3d.

All deformations of the vesicle must preserve the length L. In addition, the fluid membrane is locally incompressible. This is ensured by introducing the tension $\sigma(s)$ as a Lagrange parameter. The total energy thus reads

$$\mathcal{H}[\mathbf{r}] = \mathcal{H}_\kappa[\mathbf{r}] + \int_0^L \mathrm{d}s\, \sigma(s). \tag{7}$$

From the Euler-Lagrange equations we can deduce the force acting on the membrane

$$\mathbf{f}^{\mathrm{el}} = -\frac{\delta\mathcal{H}[\mathbf{r}]}{\delta\mathbf{r}} = \mathbf{t}\sigma' + \mathbf{n}\left(\frac{\kappa}{2}k^3 + \kappa k'' - k\sigma\right). \tag{8}$$

Here the prime denotes a derivative with respect to the arc length s.

2.2 Stokes flow

The elastic forces given by equation (8) are balanced by hydrodynamic forces mediated by the surrounding fluid. The motion of the fluid and the vesicle is only considered on time scales on which the fluid is incompressible, *i.e.*

$$\boldsymbol{\nabla} \cdot \mathbf{v} = 0. \tag{9}$$

The length and time scales in typical experiments and simulations is such that the Reynolds number is very small. We only consider fluctuations on time scales on which the inertial term in the Navier-Stokes equation can be neglected. Although we could start from the steady stochastic Stokes equation [36], we first consider the deterministic Stokes equation in the absence of thermal noise.

$$-\boldsymbol{\nabla}p + \eta_\alpha \Delta\mathbf{v} = 0. \tag{10}$$

Here $\alpha \in \{\mathrm{in}, \mathrm{out}\}$ indicates the inner or outer fluid. After deriving the deterministic equations of motion, we add stochastic noise heuristically by adding a noise term. We *assume* that noise obeys the same statistics as in equilibrium. Comparison with simulation data will show that this assumption is justified. At the vesicle membrane we must have force balance between the hydrodynamic force and the elastic forces

$$\mathbf{f}^{\mathrm{el}} + [\mathbf{T}_{\mathrm{out}} - \mathbf{T}_{\mathrm{in}}] \cdot \mathbf{n} = 0. \tag{11}$$

Here, $\mathbf{T}$ denotes the deterministic hydrodynamic stress tensor with Cartesian components

$$T_{ik} \equiv -p\delta_{ik} + \eta_\alpha[\partial_i v_k + \partial_k v_i]. \tag{12}$$

Far away from the vesicle the velocity field assumes the externally given values

$$\mathbf{v}(\mathbf{x}) \to \mathbf{v}^\infty(\mathbf{x}), \quad |\mathbf{x}| \to \infty, \tag{13}$$

which is ensured by separating an induced part from the velocity field

$$\mathbf{v} \equiv \mathbf{v}^\infty + \mathbf{v}^{\mathrm{ind}}, \tag{14}$$

and requiring that the induced part drops to zero far away from the vesicle. Assuming no-slip boundary conditions, the vesicle is advected by the flow, which implies

$$\partial_t \mathbf{r}(s,t) = \mathbf{v}(\mathbf{r}(s,t),t). \tag{15}$$

Here the dynamics still depends implicitly on $\sigma(s)$, which has to be chosen such that s remains the arc length, ensuring incompressibility. Equations (8, 10–15) determine the stochastic motion of the vesicle.

3 Quasi-circular approximation

These equations can be simplified considerably if we restrict ourselves to vesicle shapes close to the circle. We parameterize the shapes as a function of the polar angle ϕ

$$\mathbf{r}(\phi) = R_0\mathbf{e}_r(\phi)(1 + u(\phi)), \tag{16}$$

and consider small distortions u. The deformation amplitude $u(\phi)$ is a real periodic function of ϕ and can therefore be expanded into complex Fourier modes

$$u(\phi) \equiv \sum_{m=-\infty}^{\infty} u_m \frac{\exp(im\phi)}{\sqrt{2\pi}}. \tag{17}$$

The constraints and equations of motion are now expanded in terms of the amplitudes u_m. Since the technical details are rather intricate, we summarize the physically important aspects here and refer the reader to the Appendix for the details.

Area conservation is used to eliminate the u_0 mode from the expansion. The excess length then reads

$$\Delta = \frac{1}{2} \sum_{m\neq 0} (m^2 - 1)\, |u_m|^2. \tag{18}$$

The global length constraint (18) is added with a Lagrangian multiplier

$$\Sigma \equiv \kappa\sigma/R_0^2 \tag{19}$$

to the quadratic part of the bending energy. This leads to a quadratic expression for the total energy (7)

$$\mathcal{H} = \frac{\kappa}{2R_0} \sum_{m\neq 0} E_m(\sigma)|u_m|^2. \tag{20}$$

with

$$E_m(\sigma) \equiv (m+1)(m-1)[m^2 - 3/2 + \sigma]. \tag{21}$$

The bending moments and the homogeneous tension contribute a purely normal part of the elastic forces

$$f_m^{el,\kappa} = -\frac{\kappa}{R_0^2} E_m(\sigma)u_m, \tag{22}$$

while the position-dependent part of the tension gives rise to both normal and tangential forces, which are obtained from equation (8).

We now calculate the resulting velocity field of the fluid. Technically, this is achieved by expanding the flow field in terms of fundamental solutions of Stokes' equations (10) and imposing the force balance (11) at the circular membrane. In this expansion, we exclude constant external flow to avoid the Stokes paradox [37]: For viscous 2d flow around a disc no solution of the Stokes equations exist which satisfies the boundary conditions on the disc surface and at infinity. Since the effect of the disc extends to very large distances, where the Reynolds number becomes of the order of unity, inertial effects can no longer be neglected. While this paradox can be resolved using matched asymptotic expansions to the far field, this is outside the scope of the present treatment. The position-dependent part of the tension is determined from the local incompressibility condition, while the homogeneous tension σ must be determined self-consistently to preserve the global length constraint (18). The details of the calculations are given in the Appendix.

In a quiescent fluid the flow induced by the elastic forces at the membrane in Fourier space reads

$$v_m = (1/\eta_{\text{out}})\Gamma_m f_m^{el}, \qquad (23)$$

where

$$\Gamma_m \equiv \frac{|m|}{2(\lambda+1)(m^2-1)} \qquad (24)$$

is the mobility. The external flow also contributes to the flow field, both directly and via hydrodynamic forces. Finally, the membrane is advected with the flow. The resulting advection equation reads (cf. Ref. [22])

$$\partial_t u_m = i\Omega m u_m - (\kappa/\eta_{\text{out}} R_0^3)\Gamma_m E_m(\sigma)u_m + D_m \Phi_m^\infty, \quad (25)$$

with

$$D_m \equiv \frac{2m}{\lambda+1}. \qquad (26)$$

Here, Φ_m^∞ is the expansion coefficient of the external flow into fundamental modes and is given for linear shear flow

$$\mathbf{v}^\infty \equiv \dot{\gamma}y\mathbf{e}_x \qquad (27)$$

by equation (A.13). In the following, we will also use the dimensionless shear rate

$$\chi \equiv \dot{\gamma}\frac{\eta_{\text{out}} R_0^3}{\kappa} \qquad (28)$$

and vorticity

$$\tilde{\Omega} \equiv \Omega\frac{\eta_{\text{out}} R_0^3}{\kappa} = -\frac{\chi}{2}. \qquad (29)$$

At non-zero temperature, thermal noise becomes important. The force balance must then be supplemented by thermal forces. The deterministic equation of motion (25) then becomes a Langevin equation

$$\partial_t u_m = i\Omega m u_m - (\kappa/\eta_{\text{out}} R_0^3)\Gamma_m E_m(\sigma)u_m + D_m \Phi_m^\infty + \zeta_m. \tag{30}$$

The form of the thermal noise ζ_m can in principle be obtained directly from the stochastic hydrodynamic equations. It is much easier, however, to determine ζ_m from the Einstein relation, which must be valid in equilibrium. We assume that the equilibrium noise is valid also for non-vanishing shear flow and choose

$$\langle\zeta_m(t)\zeta_{m'}(t')\rangle = 2(k_B T\Gamma_m/\eta_{\text{out}} R_0^3)\delta_{m,-m'}\delta(t-t'). \quad (31)$$

Equation (30) is the correct stochastic equation of motion for the vesicle deformation modes u_m. The tension σ is at each instance determined such that the length constraint (18) is fulfilled. Taking the time derivative of equation (18) and using equation (30), we can solve for the tension

$$\sigma = \left[\sum_{m\neq0}(m^2-1)^2\Gamma_m|u_m|^2\right]^{-1}\sum_{m\neq0}(m^2-1)\Big[i\Omega m|u_m|^2$$
$$-\frac{\kappa}{\eta_{\text{out}} R_0^3}\Gamma_m E_m(0)|u_m|^2 + D_m u_m^*\Phi_m^\infty + u_m^*\zeta_m\Big]. \quad (32)$$

When this expression is inserted back into equation (30), the resulting noise term becomes dependent on the instantaneous values of the u_m. While such non-linear noise terms hold interesting physics, we first concentrate on tractable approximate solutions to the stochastic equation of motion.

4 Approximate solutions

4.1 Mean-field treatment

At finite temperature, higher-order modes are excited by stochastic thermal forces and therefore cannot be neglected. The full non-linear set of Langevin equations (30) in combination with the expression (32) for σ is too complex to admit a general solution. We can, however, gain further insight in the tank-treading regime using a mean-field description. We replace the fluctuating tension σ in equation (30) by a constant, which has to be determined self-consistently from the length constraint. The Langevin equations (30) then become linear and decouple. In the stationary state, only the $m=2$ deformations have a finite mean,

$$\langle u_2\rangle = \frac{\eta_{\text{out}} R_0^3}{\kappa}\frac{D_2\Phi_2^\infty}{\Gamma_2 E_2(\sigma)+i\chi}. \qquad (33)$$

The terms in this equation can be interpreted physically as follows. The elongational part of the external flow, proportional to Φ_2^∞, stretches the vesicle. The combination of bending moments and tensile force, given by the $E_2(\sigma)$ term, counteracts this stretching. Competing with the elastic force is the advection term $i\chi$ arising from the rotational part of the external flow. For a given amplitude $|\langle u_2\rangle|$ the tension must scale like $E_2(\sigma) \sim (-5/2+\sigma) \sim \chi$.

On average, the vesicle is elliptical. As a measure of the deformation from the circle we define the Taylor deformation parameter

$$D \equiv \frac{L-S}{L+S}, \tag{34}$$

where L and S denote the long and short axis of the ellipse. In the mean-field treatment we have

$$D = \frac{2}{3} \frac{\chi}{[(5/2+\sigma)^2 + 9\chi^2(1+\lambda)^2]^{1/2}}. \tag{35}$$

The inclination angle is obtained from equation (33)

$$\Theta = \frac{1}{2} \arctan \frac{5/2+\sigma}{\chi(1+\lambda)}. \tag{36}$$

The deviations from the mean

$$\delta u_m \equiv u_m - \langle u_m \rangle \tag{37}$$

obey the homogeneous Langevin equation

$$\partial_t \delta u_m = im\Omega \delta u_m - (\kappa/\eta_{\text{out}} R_0^3) \Gamma_m E_m(\sigma) \delta u_m + \zeta_m. \tag{38}$$

The stationary noise correlations are best evaluated using a time Fourier transform

$$\widehat{\delta u}(\omega) \equiv \int dt \exp(-i\omega t)\delta u(t), \tag{39}$$

leading to

$$i\omega \widehat{\delta u}_m = -im\Omega \widehat{\delta u}_m - (\kappa/\eta_{\text{out}} R_0^3)\Gamma_m E_m(\sigma)\widehat{\delta u}_m + \widehat{\zeta}_m. \tag{40}$$

We can solve for $\widehat{\delta u}_m(\omega)$ and obtain the correlations

$$\langle \widehat{\delta u}_m(\omega)\widehat{\delta u}_{-m}(-\omega) \rangle = \frac{2k_B T \Gamma_m/\eta_{\text{out}} R_0^2}{(\omega + m\Omega)^2 + \left[\frac{\kappa \Gamma_m E_m}{\eta_{\text{out}} R_0^3}\right]^2}. \tag{41}$$

We have left the σ-dependence of E_m implicit for clarity. The time correlation function becomes ($\Delta t > 0$)

$$\langle \delta u_m(0)\delta u_{-m}(\Delta t) \rangle =$$
$$\int \frac{d\omega}{2\pi} \exp(i\omega\Delta t)\langle \widehat{\delta u}_m(\omega)\widehat{\delta u}_{-m}(-\omega)\rangle =$$
$$\frac{k_B T R_0}{\kappa E_m} \exp\left[-\left(\frac{\kappa \Gamma_m E_m}{\eta_{\text{out}} R_0^3} + im\Omega\right)\Delta t\right], \tag{42}$$

with the stationary equal-time correlations

$$\langle \delta u_m(t)\delta u_{-m}(t) \rangle = \frac{k_B T R_0}{\kappa E_m(\sigma)}. \tag{43}$$

The amplitudes u_m with different m are uncorrelated at all times. The equal-time correlations are identical with the equilibrium spectrum. However, the tension σ is determined by the non-equilibrium conditions.

The fluctuating u_m contribute to the excess length according to equation (18). Although the length constraint cannot be obeyed exactly with a constant tension, we determine σ such that the constraint (18) is fulfilled on average. The total excess length has a systematic and a fluctuating part

$$\Delta = \bar{\Delta}(\sigma) + \sum_{m \geq 2} \Delta_m(\sigma), \tag{44}$$

with

$$\bar{\Delta}(\sigma) \equiv \sum_{m>0}(m^2-1)\frac{D_m^2|\Phi_m^\infty|^2}{\Gamma_m^2 E_m(\sigma)^2 + m^2\tilde{\Omega}^2}$$
$$= \frac{3\pi}{2}\frac{\chi^2}{(5/2+\sigma)^2 + \chi^2(1+\lambda)^2} \tag{45}$$

and

$$\Delta_m(\sigma) \equiv (m^2-1)\langle|\delta u_m|^2\rangle = \frac{k_B T R_0}{\kappa(m^2 - 3/2 + \sigma)}. \tag{46}$$

Thus σ is determined implicitly by the solution of equation (44). For future reference, we note that the contribution of the fluctuating parts to the excess length can be determined analytically to be

$$\sum_{m\geq 2}\Delta_m(\sigma) = \frac{k_B T R_0}{\kappa\sqrt{2}\,(4\sigma^2 - 8\sigma + 3)}\left[\sqrt{2}(7-6\sigma)\right.$$
$$\left. + \pi\sqrt{3-2\sigma}(2\sigma-1)\cot\left(\pi\sqrt{3/2-\sigma}\right)\right]. \tag{47}$$

While this expression is exact, its behavior as a function of σ is not obvious (for example, the "singularities" at $\sigma = 1/2$ and $\sigma = 3/2$ are only apparent). We therefore give the leading asymptotic behavior

$$\sum_{m\geq 2}\Delta_m(\sigma) \approx \frac{k_B T R_0}{\kappa}\begin{cases}1/(\sigma+5/2)+25/48, & \sigma \to -5/2, \\ \pi(4\sigma)^{-1/2}, & \sigma \to \infty.\end{cases} \tag{48}$$

We can thus identify two limiting cases. In the fluctuation-dominated regime near the tumbling instability, $\sigma \to -5/2$, the amplitude of the fluctuations with $m = 2$ become very large, while the higher-order modes store a fixed excess length. In the tension-dominated case ($\sigma \to \infty$), the excess length stored in each mode is independent of the mode number up to $m \sim \sqrt{\sigma}$, where the bending forces become larger than the tensile forces.

4.2 Zero temperature

At large shear rates, nearly the entire excess length is stored in the systematic part $\bar{\Delta}$. As a crossover shear rate χ_c, we can define the shear rate at which the two contributions in condition (44) become equal

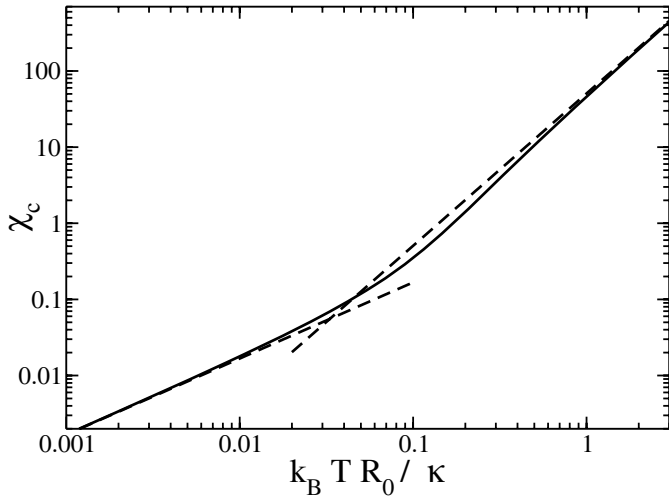$$\bar{\Delta}(\sigma, \chi_c) \equiv \sum_{m\geq 2}\Delta_m(\sigma) = \frac{\Delta}{2}. \tag{49}$$

Fig. 2. Critical shear rate χ_c *versus* reduced temperature $k_B T R_0/\kappa$. Data are obtained numerically from equation (49) for $\Delta \simeq 0.163$ and $\lambda = 1$ (straight line). The dashed lines visualizes the asymptotic scaling (50) for low and high values of the temperature, respectively. A significant portion of the excess length Δ is stored in the thermally fluctuating higher order modes $m > 2$ for $\chi < \chi_c$.

This set of equations must be solved numerically for each Δ. In the limit $\chi \gg \chi_c$ we can ignore the thermal forces. In this case, the equation of motion (30) becomes the deterministic equation (25), and the tension is determined by equation (32) with $\zeta_m = 0$. The scaling relations (48) imply

$$\chi_c \approx \frac{1}{\sqrt{3\pi - \Delta(1+\lambda)^2}}$$
$$\times \begin{cases} 2\Delta^{-1/2}\,(k_B T R_0/\kappa), & \frac{k_B T R_0}{\kappa\Delta} \ll 1, \\ \pi^2 \Delta^{-3/2}\,(k_B T R_0/\kappa)^2, & \frac{k_B T R_0}{\kappa\Delta} \gg 1. \end{cases} \quad (50)$$

A plot of χ_c as a function of reduced temperature together with the asymptotic scaling laws is shown in Figure 2.

We can easily obtain the stationary state from $\partial_t u_m^0 = 0$, *i.e.*

$$u_m^0 = \frac{\eta_{\text{out}} R_0^3}{\kappa} \frac{D_m}{\Gamma_m E_m(\sigma_0) + im\tilde{\Omega}} \Phi_m^\infty. \quad (51)$$

The homogeneous tension σ_0 is determined from the length constraint (18). In the case of constant linear shear flow, only the $m = \pm 2$ components are non-zero and are equal in magnitude. The length constraint thus reads $|u_{\pm 2}| = (\Delta/3)^{1/2}$, or

$$\Delta = 3\frac{D_2^2}{\Gamma_2^2 E_2^2 + 4\Omega^2}\frac{2\pi\chi^2}{64}$$
$$= \frac{3\pi}{2(1+\lambda)^2}\frac{\chi^2}{(5/2+\sigma_0)^2/(9(1+\lambda))^2 + \chi^2}. \quad (52)$$

The homogeneous tension in the stationary state is thus given by

$$\sigma_0 = -5/2 + 3\chi(1+\lambda)\left[\frac{3\pi}{2\Delta(1+\lambda)^2} - 1\right]^{1/2}. \quad (53)$$

We see that in the large shear rate limit the tension grows as $\sigma \sim \chi$ to counteract the stretching of the elongational flow. The stationary solution becomes unstable when E_2 vanishes, which happens at a critical viscosity ratio

$$\lambda_c = \sqrt{\frac{3\pi}{2\Delta}} - 1. \quad (54)$$

This corresponds to a tank-treading to tumbling transition, as can be seen when we allow for time-dependent σ_0: In linear shear flow, only the $m = 2$ modes are excited. In the long time limit we can therefore assume that all other modes have decayed. In analogy with the 3d treatment [18], we can write u_2 in polar form

$$u_2 \equiv (\Delta/3)^{1/2}\exp(-2i\Theta), \quad (55)$$

where Θ is the inclination angle of the vesicle with respect to the shear direction. Taking the real and imaginary part of equation (25) gives the familiar Jeffery's equation [38]

$$\dot{\Theta} = \dot{\gamma}\left[-\frac{1}{2} + \frac{1}{2}\frac{\sqrt{3\pi}}{(\lambda+1)\sqrt{2\Delta}}\cos(2\Theta)\right]. \quad (56)$$

For $\lambda < \lambda_c$, equation (56) admits two stationary solutions, of which only the positive is linearly stable

$$\Theta_0 \equiv \frac{1}{2}\arccos\left(\frac{(\lambda+1)^2 2\Delta}{3\pi}\right)^{1/2}. \quad (57)$$

This corresponds to stationary tank-treading motion, where the tank-treading frequency at zeroth order is given by the external flow

$$\omega_{\text{tt}}^{\text{QC}} \equiv \frac{\dot{\gamma}}{2}. \quad (58)$$

For $\lambda > \lambda_c$, the right-hand side of equation (56) is always negative, and the vesicle starts to tumble. In two dimensions, no analogy to a swinging motion (cf. Refs. [18,16, 19,20]) exists, since the volume and length constraint already uniquely determine the shape of an ellipse.

4.3 First-order correction to the large shear-rate limit

In the mean-field approach the tension σ is assumed constant and all modes fluctuate independently with amplitudes given by equation (43). In this picture, the length constraint is not fulfilled rigorously but only on average. For strictly enforced length constraint the tension must fluctuate according to equation (32), which induces correlations between the deformation amplitudes. While this general effect is worth considering in its own right, here we concentrate on the much simpler large shear rate (or low temperature) limit as a perturbation of the deterministic solution.

At $T = 0$, the whole excess length Δ is stored in the $|m| = 2$ mode. Perturbing the modulus of the amplitude $|u_2|$ alters the excess length Δ to first order and is prohibited by the constraint (2). Perturbing the other modes

alters Δ only to second order. At low temperature, we can therefore assume the polar decomposition (55). Taking the real and imaginary part of the equation of motion (30), we arrive at a Langevin equation for the inclination angle

$$\dot{\Theta} = \dot{\gamma}\left[-\frac{1}{2} + \frac{1}{2}\frac{\sqrt{3\pi}}{(\lambda+1)\sqrt{2\Delta}}\cos(2\Theta)\right] + \xi, \qquad (59)$$

where the noise term

$$\xi \equiv \sqrt{\frac{3}{4\Delta}}\,\text{Im}[\zeta_2\exp(2i\Theta)] \qquad (60)$$

is Gaussian and delta-correlated

$$\langle\xi(t)\xi(0)\rangle = \frac{3}{4\Delta}\Gamma_2 k_B T\delta(t). \qquad (61)$$

In the stationary regime Θ fluctuates around the mean value

$$\Theta \equiv \Theta_0 + \Delta\Theta, \qquad (62)$$

where Θ_0 is given by equation (57). For small $\Delta\Theta$ we can expand equation (59) to obtain

$$\dot{\Delta\Theta} = -\dot{\gamma}\sqrt{\frac{2\pi}{3\Delta}}\frac{1}{\lambda+1}\sin(2\Theta_0)\Delta\Theta + \xi. \qquad (63)$$

This implies the stationary correlations

$$\langle\Delta\Theta^2\rangle = \frac{R_0 k_B T}{\kappa\chi\Delta^{1/2}}\frac{1}{8}\left[\frac{3\pi}{2} - (\lambda+1)^2\Delta\right]^{-1/2} = \frac{3k_B T R_0}{8\kappa\Delta E_2(\sigma_0)}, \qquad (64)$$

where we have used equation (57). For small Δ we read off

$$\langle\Delta\Theta^2\rangle^{1/2} \approx \left(\frac{1}{129\pi}\right)^{1/4}\left(\frac{\kappa\chi\Delta^{1/2}}{R_0 k_B T}\right)^{-1/2}$$

$$\approx 0.20\left(\frac{\kappa\chi\Delta^{1/2}}{R_0 k_B T}\right)^{-1/2}. \qquad (65)$$

5 Keller-Skalak theory

In order to compare with numerical simulation data, we present a second, deterministic theoretical description of the motion of vesicles, which takes into account the influence of the vesicle shape on the flow. In the theory of Keller and Skalak [32], a three-dimensional vesicle is assumed to have a fixed ellipsoidal shape

$$(x_1/a_1)^2 + (x_2/a_2)^2 + (x_3/a_3)^2 = 1, \qquad (66)$$

where the a_i are the semi-axes of the ellipsoid, and the coordinate axes x_i point along its principal directions. The x_1 and x_2 axes, with $a_1 > a_2$, are chosen to lie in the xy plane and are rotated through an angle Θ with respect to the x and y axes. The components of the undisturbed shear flow are $(\dot{\gamma}y, 0, 0)$. The velocity field at the membrane is assumed to be

$$\mathbf{v} = \omega_{\text{tt}}^{\text{KS}}\left(-(a_1/a_2)x_2, (a_2/a_1)x_1, 0\right), \qquad (67)$$

where $\omega_{\text{tt}}^{\text{KS}}$ is a parameter having the dimensions of a frequency. The energy supplied by the external flow has to be balanced with the energy dissipated inside the vesicle. The motion of the vesicle derived from this energy balance reads [32]

$$\frac{d\Theta}{dt} = -\frac{\dot{\gamma}}{2} + \dot{\gamma}B\cos(2\Theta), \qquad (68)$$

with

$$B = \frac{1}{1+r_2^2}\left\{\frac{(1-r_2^2)^2[z_2(1-\lambda)-2]-8r_2^2}{2(1-r_2^2)[z_2(1-\lambda)-2]}\right\} \qquad (69)$$

and

$$\omega_{\text{tt}}^{\text{KS}} = 2\dot{\gamma}\frac{r_2(1+r_2^2)}{(1-r_2^2)^2[z_2(1-\lambda)-2]-8r_2^2}. \qquad (70)$$

The factors appearing in equations (68–70) are given by

$$r_2 \equiv a_2/a_1, \qquad r_3 \equiv a_3/a_1, \qquad z_2 \equiv g_3'(\alpha_1^2 + \alpha_2^2),$$
$$\alpha_1 \equiv r_2^{-1/3}r_3^{-1/3}, \quad \alpha_2 \equiv r_2^{2/3}r_3^{-1/3}, \quad \alpha_3 \equiv r_2^{-1/3}r_3^{2/3}, \qquad (71)$$

and

$$g_3' \equiv \int_0^\infty (\alpha_1^2 + s)^{-3/2}(\alpha_2^2 + s)^{-3/2}(\alpha_3^2 + s)^{-1/2}ds. \qquad (72)$$

For $B > 1/2$, we obtain a steady tank-treading angle

$$\Theta = \frac{1}{2}\arccos\left(\frac{1}{2B}\right). \qquad (73)$$

We calculate the inclination angle Θ and the tank-trading frequency $\omega_{\text{tt}}^{\text{KS}}$ by adapting the Keller-Skalak theory to two dimensions. We numerically solve equations (68–70) in the limit $r_3 \to +\infty$ keeping r_2 finite, which formally corresponds to an ellipsoid with an infinite semi-axis in the z-direction.

6 Simulation method

A 2d vesicle model system was simulated using the multi-particle collision (MPC) dynamics [23,5,26]. In this method the fluid is not treated on a continuum level, but rather by a stochastic dynamics of effective fluid particles.

6.1 Solvent dynamics

We consider a two-dimensional system made of N_s identical particles of mass m_s whose positions $\mathbf{r}_i(t)$ and velocities $\mathbf{v}_i(t)$, $i = 1, 2, \ldots, N_s$, are continuous variables. The time is discretized in intervals Δt_s. The evolution occurs in two consecutive steps, streaming and collision. In the streaming step, particles move ballistically,

$$\mathbf{r}_i(t + \Delta t_s) = \mathbf{r}_i(t) + \mathbf{v}_i(t)\Delta t_s. \qquad (74)$$

For the collision step, the system is divided into the cells of a regular square lattice of mesh size a. Each of these

cells is the interaction area where an instantaneous multi-particle collision occurs, which changes particles velocities as [23]

$$\mathbf{v}_i(t + \Delta t_s) = \mathbf{u}(t) + \Omega[\mathbf{v}_i(t) - \mathbf{u}(t)], \qquad (75)$$

where $\mathbf{u}$ is the average velocity of the colliding particles in a cell. The velocity field $\mathbf{u}$ is considered to be the macroscopic velocity of the fluid and it is assumed to have the coordinates of the center of the cell. Ω denotes a stochastic rotation matrix which rotates, with equal probability, by an angle of either $+\alpha$ or $-\alpha$. The collisions are performed simultaneously on all the particles in a cell with the same rotation Ω, but Ω may differ from cell to cell. The local momentum and kinetic energy are conserved under this dynamics. The kinetic energy of particles fixes the temperature $k_B T$, where k_B is the Boltzmann constant, via the equipartition theorem.

It was shown in reference [39] that a proper description of hydrodynamics in MPC requires large Schimdt numbers. This can be accomplished by choosing a mean-free path $l = \Delta t_s \sqrt{k_B T / m_s}$, which is small compared to the cell size a. It is known that a value of l much smaller than a breaks the Galilean invariance [40] and that this problem can be solved by applying a random shift procedure [40]. The viscosity of the solvent fluid is [25,41]

$$\eta = \left[\frac{l}{2a} \left[\frac{n_c^2}{(n_c - 1 + e^{-n_c}) \sin^2 \alpha} - n_c \right] \right. $$
$$\left. + \frac{a}{12l}(n_c - 1 + e^{-n_c})(1 - \cos \alpha) \right] \frac{\sqrt{m_s k_B T}}{a}, \qquad (76)$$

with particle density $\rho = n_c m_s / a^2$ and number n_c of particles per cell.

In order to enforce shear flow, we place our system of size $L_x \times L_y$ between two horizontal walls. The upper and the lower walls slide along the x-direction with velocities $\mathbf{v}_{wall} = (v_{wall}, 0)$ and $-\mathbf{v}_{wall}$, respectively, with $v_{wall} > 0$. Periodic boundary conditions are used along the x-direction. Along the y-direction, we use a modified bounce-back boundary condition which consists in requiring that particles hitting the walls change their velocities according to $\mathbf{v}_i \rightarrow 2\mathbf{v}_{wall} - \mathbf{v}_i$. Together with virtual particles in partly filled cells at walls, this describes no-slip boundary conditions very well [27,28]. A linear flow profile $(u_x, u_y) = (\dot{\gamma}y, 0)$ is obtained with shear rate $\dot{\gamma} = 2v_{wall}/L_y$, with the walls placed at $y = \pm L_y/2$. The relative velocities in the collision cells are rescaled after each time step Δt_s in order to keep the temperature constant in the (driven) system.

6.2 Membrane model

The vesicle membrane is modeled by connecting N_p beads of mass m_p successively with bonds into a closed ring. Neighboring beads along the closed chain are connected to each other with the harmonic potential

$$U_{\text{bond}} \equiv \frac{k_h}{2} \sum_{i=1}^{N_p} \frac{(|\mathbf{r}_i - \mathbf{r}_{i-1}| - r_0)^2}{r_0^2}, \qquad (77)$$

where k_h is a spring constant, $\mathbf{r}_i$ is the position vector of the i-th bead, and r_0 is the average bond length. The bending energy (A.4) is modeled on the discrete level by a bending potential

$$U_{\text{bend}} \equiv \frac{\kappa}{r_0} \sum_{i=1}^{N_p} (1 - \cos \beta_i), \qquad (78)$$

where β_i is the angle between successive bonds. The fluid modeled with the MPC method is compressible. To enforce the area constraint in the presence of thermal and hydrodynamic forces, we add a constraint potential

$$U_{\text{area}} \equiv \frac{k_A}{2} \frac{(A - A_0)^2}{r_0^4}. \qquad (79)$$

6.3 Coupling of membrane and solvent dynamics

The membrane-solvent interaction must prevent solvent particles from crossing the membrane and enforce no-slip boundary conditions on the membrane. Therefore we place hard disks centered on the membrane beads. The disk radius r_p is set in order to ensure overlapping of disks and a complete coverage of the membrane. The exchange of momentum between the solvent particles and the membrane occurs in the following way. After updating beads positions and velocities via molecular dynamics (MD), we freely stream all the solvent particles. We then execute bounce-back scattering between solvent and membrane disks only when a solvent particle j and a disk i satisfy the conditions $|\mathbf{r}_i - \mathbf{r}_j| < r_p$ and $(\mathbf{r}_i - \mathbf{r}_j) \cdot (\mathbf{v}_i - \mathbf{v}_j) < 0$. This means that if the two collision partners i and j overlap and move towards each other, then their velocities are updated according to

$$\mathbf{v}_i \rightarrow \mathbf{v}_i - 2\frac{m_s}{m_s + m_p}(\mathbf{v}_i - \mathbf{v}_j),$$
$$\mathbf{v}_j \rightarrow \mathbf{v}_j + 2\frac{m_p}{m_s + m_p}(\mathbf{v}_i - \mathbf{v}_j). \qquad (80)$$

To avoid that a solvent particle moves too far inside a disk, we require that $l \ll r_p$. The collision step (75) is performed only on those solvent particles which did not scatter. If the collision step were executed also on the scattered solvent particles, they might continue to collide with the same disk in the next time step. The fluids in the interior and exterior of the vesicle are taken to be the same, in particular to have the same viscosity.

A chain of disks of finite radius r_p has an inner length available to the solvent particles which is smaller than the outer length. Since the solvent has the same density inside and outside, the outer fluid exerts a compression force on the membrane until the inner density increases so that an expansion force compensates the compression one. It is straightforward to show [6] that the density increase is $\Delta \rho / \rho = 2r_p / R^*$ where $2r_p$ is the effective membrane thickness. This requires that R_0 is large enough compared to the disk radius r_p to reduce such compression effects. The

number of solvent particles placed inside the vesicle fixes an average area. However, since the MPC fluid is compressible, shear and bending rigidity effects may change the area A. For this reason the constraint potential (79) is introduced to keep the area constant.

6.4 Parameters

In experiments with vesicles in shear flow, inertial effects are negligible since the Reynolds number $Re \equiv \dot{\gamma}\rho R^{*2}/\eta_{\text{out}}$ is very small. We express our results using the reduced area $A^* = A_0/\pi R^{*2}$, defined in equation (4), and the reduced shear rate $\chi = \dot{\gamma}\eta_{\text{out}}R_0^3/\kappa$, see equation (28), as relevant dimensionless quantities.

We set $\alpha = \pi/4$, $n_c = 10$, and $l = 0.008a$. This implies a viscosity $\eta_{\text{out}} = \eta_{\text{in}} \simeq 28.0\sqrt{m_s k_B T}/a$. We use $L_x = 150a$, $L_y = 90a$, $R^* = 15.3a$, and v_{wall} such that $Re < 0.1$ for all the cases we considered with $0.5 \leq \chi \leq 10.0$. Finally, we set $m_p = 10m_s$, $N_p = 96$, $\Delta t_p = \Delta t_s/20$, $r_p = 0.9a$, $r_0 = a$, $\kappa = 40k_B T a$, $k_A = 0.5k_B T$, $k_h = 4000k_B T$. The area A_0 is chosen in such a way that $0.7 \leq A^* \leq 0.95$. With the choices for k_A and k_h the area and the length of the vesicle are kept constant with a deviation of less than 1% of the target values for all simulated systems. A snapshot of a simulated vesicle and the resulting velocity field for the reduced area $A^* = 0.95$ and reduced shear rate $\chi = 5.6$ is shown in Figure 1.

7 Results and discussion

Comparing analytic predictions with simulation data is facilitated by using real Fourier coefficients. In this section we therefore employ the real Fourier series

$$u(\phi) \equiv a_0 + \sum_{m=1}^{\infty} a_m \cos(m\phi) + \sum_{m=1}^{\infty} b_m \sin(m\phi), \quad (81)$$

rather than the complex expansion (17). The real Fourier coefficients a_m, b_m are connected with the complex Fourier coefficients u_m via ($m \neq 0$)

$$u_m = \sqrt{\frac{\pi}{2}} \left(a_m - ib_m\right). \quad (82)$$

The corresponding correlations now read

$$\langle \delta a_m(0)\delta a_m(t)\rangle = \langle b_m(0)b_m(t)\rangle =$$
$$\frac{k_B T R_0}{\pi \kappa E_m} \exp\left(-\frac{\kappa \Gamma_m E_m}{\eta_{\text{out}} R_0^3}t\right) \cos(m\dot{\gamma}t/2),$$

$$\langle \delta a_m(0)\delta b_m(t)\rangle = -\langle b_m(0)a_m(t)\rangle =$$
$$\frac{k_B T R_0}{\pi \kappa E_m} \exp\left(-\frac{\kappa \Gamma_m E_m}{\eta_{\text{out}} R_0^3}t\right) \sin(m\dot{\gamma}t/2)$$

$$(83)$$

and

$$\langle \delta a_m(0)\delta a_m(0)\rangle = \langle \delta b_m(0)\delta b_m(0)\rangle = \frac{k_B T R_0}{\pi \kappa E_m(\sigma)},$$
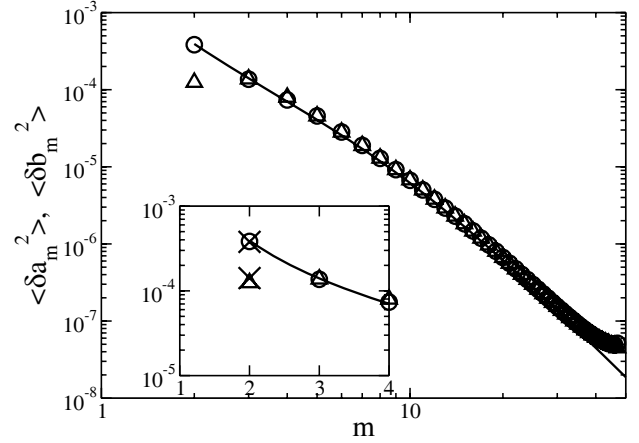$$\langle \delta a_m(0)\delta b_m(0)\rangle = 0. \quad (84)$$

Fig. 3. Stationary correlations $\langle \delta a_m^2\rangle$ (triangles) and $\langle \delta b_m^2\rangle$ (circles) as a function of mode number m on a double logarithmic scale. The solid line corresponds to a fit of equation (84) with $\Sigma_{\text{fit}} \simeq 103\kappa/R_0^2$. The inset highlights $\langle \delta a_2^2\rangle$, $\langle \delta b_2^2\rangle$ in comparison with the low-temperature expansion equation (86) (crosses). Simulation parameters are $\Delta = 0.163$ (corresponding to $A^* = 0.95$) and $\chi \simeq 9.3$. Deviations from the fit for $m \geq 40$ are due to the finite bond length r_0 in the discretized vesicle membrane, below which continuum theory no longer applies [42], and to numerical noise, which leads to a constant background.

Finally, we calculate the fluctuations of the Fourier modes a_2, b_2 in the large shear rate limit, cf. Section 4.3. The polar expansion (55) implies

$$a_2 = \sqrt{\frac{2\Delta}{3\pi}} \cos(2\Theta),$$
$$b_2 = \sqrt{\frac{2\Delta}{3\pi}} \sin(2\Theta). \quad (85)$$

We derive the correlation functions of the $m = 2$ modes from equation (64) to be

$$\langle \delta a_2\delta a_2\rangle = \frac{k_B T R_0}{\pi \kappa E_2(\sigma_0)} \cos^2(2\Theta_0),$$
$$\langle \delta a_2\delta b_2\rangle = \frac{k_B T R_0}{\pi \kappa E_2(\sigma_0)} \cos(2\Theta_0)\sin(2\Theta_0), \quad (86)$$
$$\langle \delta b_2\delta b_2\rangle = \frac{k_B T R_0}{\pi \kappa E_2(\sigma_0)} \sin^2(2\Theta_0).$$

In Figure 3 we show the stationary deformation correlations $\langle \delta a_m^2\rangle$, $\langle \delta b_m^2\rangle$ as a function of the mode number m for $\Delta = 0.163$ and $\chi \simeq 9.3$. We also show a fit of these correlations for $m \geq 3$ with the theoretical prediction (84). From the fit we can extract the tension Σ. In this particular example we obtain $\Sigma_{\text{fit}} \simeq 103\kappa/R_0^2$, whereas theory predicts $\Sigma_{\text{theor}} \simeq 113\kappa/R_0^2$ from equations (44–46).

The mean-field treatment (84) predicts $\langle \delta a_m^2\rangle = \langle \delta b_m^2\rangle$ for all m. We can see that this holds only for $m \geq 3$. As explained in Section 4.3, this is due to the fluctuations in the line tension. In the inset of Figure 3, we compare $\langle \delta a_2^2\rangle$,
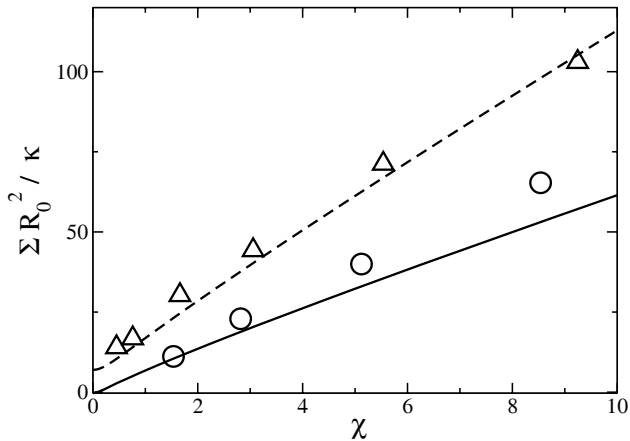
Fig. 4. Dimensionless tension $\Sigma R_0^2/\kappa$ as a function of reduced shear rate χ. Symbols denote the fitted tensions σ_{fit} extracted from fluctuation spectra for excess lengths $\Delta = 0.163$ (triangles) and $\Delta = 0.340$ (circles), corresponding to $A^* = 0.95$ and $A^* = 0.9$, respectively (compare Fig. 3). The solid and dashed lines show the corresponding numerical solution of equations (44–46).

$\langle\delta b_2^2\rangle$ with the low temperature expansion (86), with very good agreement.

Figure 4 shows the extracted dimensionless tensions $\Sigma_{\text{fit}} R_0^2/\kappa$ for different dimensionless shear rates $0 \leq \chi \leq 10$ and for two different excess lengths $\Delta = 0.163$ and $\Delta = 0.340$. The agreement with the theoretical prediction from a numerical solution of equations (44–46) is satisfactory. The fact that this function is nearly a straight line implies that the large-shear-rate approximation (12) is valid down to small shear rates. We find a crossover shear rate χ_c, below which there are deviations from a linear behavior. Theoretically, equation (49) gives an order-of-magnitude estimate of $\chi_c \simeq 3.09$ for $\Delta = 0.163$ and $\chi_c \simeq 0.99$ for $\Delta = 0.340$.

In Figure 5, the time autocorrelation function $\langle a_3(t)a_3(0)\rangle$ is shown as a function of dimensionless time $\dot{\gamma}t$. The data follows the expected exponential decay (83) very well. From the amplitude $\langle\delta a_3(0)\delta a_3(0)\rangle$ we can extract a tension $\Sigma \simeq 65\kappa/R_0^2$, while from the time constant we deduce $\Sigma \simeq 44\kappa/R_0^2$. Theory predicts $\Sigma_{\text{theor}} \simeq 73\kappa/R_0^2$. Given the rather noisy data, this agreement seems reasonable. For moderate shear rates the autocorrelation function has decayed before the oscillations implied by equation (83) become noticeable. Even for the large shear rate $\chi \simeq 5.6$ used in Figure 5, the oscillations are barely visible. For the same reason the build-up of cross correlation $\langle a(t)b(0)\rangle$ is hidden in the numerical noise.

We compare the averaged inclination angle $\langle\Theta\rangle$ for different reduced areas A^* with equation (57) in Figure 6, valid in the quasi-circular limit. The agreement with simulation data is satisfactory, given the large error bars. The 2d Keller-Skalak theory, which is also shown in the plot, gives slightly better agreement.

In Figure 7, we show the fluctuations of the inclination angle $\langle\Delta\Theta^2\rangle \equiv \langle\Theta^2\rangle - \langle\Theta\rangle^2$ as a function of the shear rate.
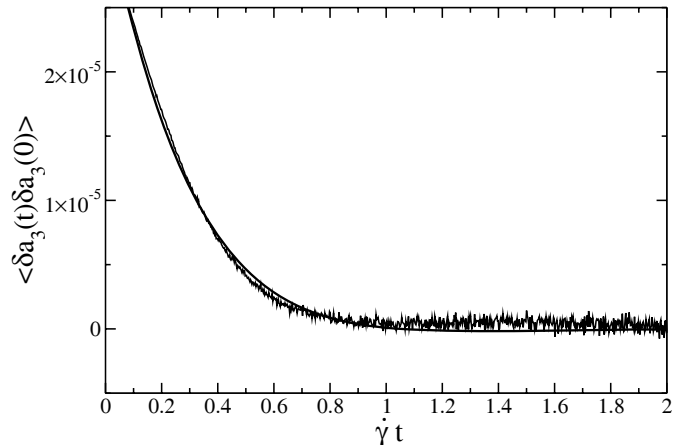

Fig. 5. Autocorrelation function $\langle\delta a_3(t)\delta a_3(0)\rangle$ of the a_3 mode as a function of dimensionless time $\dot{\gamma}t$. Simulation parameters are $\Delta = 0.163, \chi = 5.6$. The solid line shows a fit of equation (83).
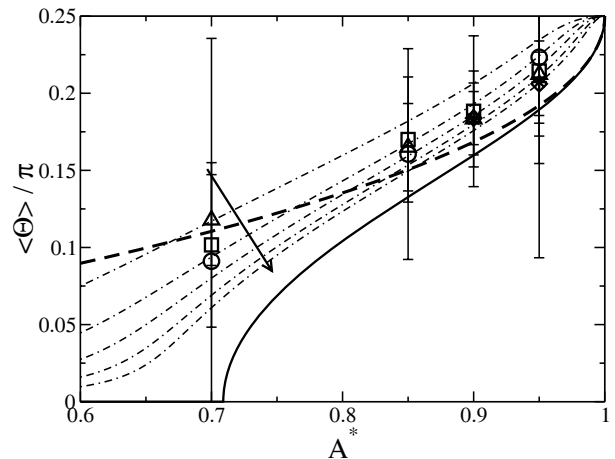

Fig. 6. Scaled average inclination angle $\langle\Theta\rangle/\pi$ as a function of reduced area A^*. Symbols with error bars show simulation data for different values of the reduced shear rate $\chi = 10.0A^{*3/2}$ (diamonds), $\chi = 6.0A^{*3/2}$ (stars), $\chi = 3.3A^{*3/2}$ (triangles), $\chi = 1.8A^{*3/2}$ (squares), $\chi = 0.8A^{*3/2}$ (circles). The continuous line corresponds to the deterministic limit equation (57) and is independent of χ. Dashed-dot lines follow from the mean-field equations (33, 36) with $\chi A^{*-3/2} \in \{0.8, 1.8, 3.3, 6, 10\}$ growing in the direction indicated by the arrow. The thick dashed line follows from the Keller-Skalak theory, see equation (73).

The theoretical scaling is given by equation (65), and is in excellent agreement for $A^* = 0.85$ ($\Delta \simeq 0.53$), $A^* = 0.9$ ($\Delta \simeq 0.34$), and $A^* = 0.95$ ($\Delta \simeq 0.163$). The scaling of the fluctuations of Θ for A^* differs significantly for $A^* = 0.7$ ($\Delta \simeq 1.23$). In the deterministic case, a vesicle with such a low reduced area would tumble within the quasi-circular theory. This implies that the quasi-circular approximation works well for $\Delta \leq 0.53$ (corresponding to $A^* \geq 0.85$) in two dimensions.

Finally, we show the rescaled tank-treading frequency $\omega_{\text{tt}}/\dot{\gamma}$ as a function of A^* in Figure 8. Again, agreement
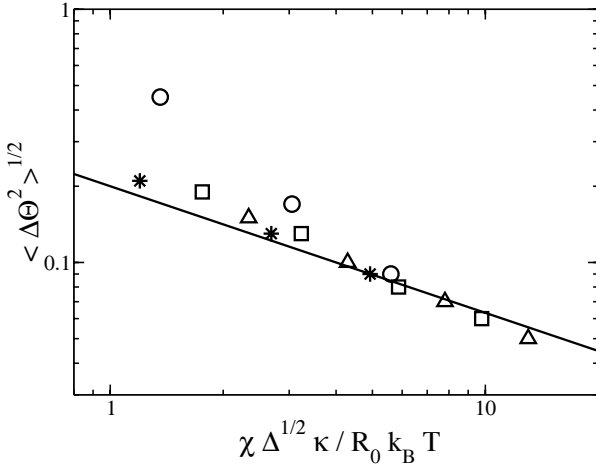
Fig. 7. Fluctuations of the inclination angle $\langle \Delta \Theta^{1/2} \rangle^{1/2}$ as a function of reduced shear rate $\chi \Delta^{1/2} \kappa/(R_0 k_B T)$. Symbols denote simulation data for different $A^* = 0.95$ (squares), $A^* = 0.90$ (triangles), $A^* = 0.85$ (stars), $A^* = 0.7$ (circles), corresponding to $\Delta \simeq 0.163$, $\Delta \simeq 0.34$, $\Delta \simeq 0.53$, and $\Delta \simeq 1.23$, respectively. The solid line is the quasi-circular scaling prediction of equation (65).
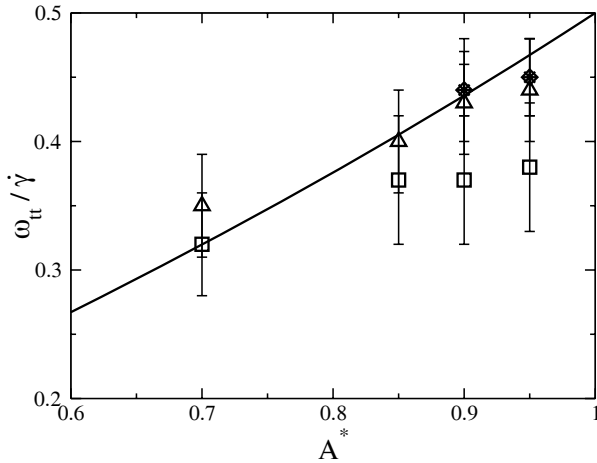

Fig. 8. Tank-treading frequency ω_{tt} rescaled by shear rate $\dot{\gamma}$, as a function of reduced area A^* for different values of the reduced shear rate $\chi = 10.0A^{*3/2}$ (diamonds), $6.0A^{*3/2}$ (stars), $3.3A^{*3/2}$ (triangles), $1.8A^{*3/2}$ (squares). The solid line follows from the Keller-Skalak theory, see equation (70).

with the 2d Keller-Skalak theory is quite good, while the quasi-circular theory neglects the effect of the vesicle shape on the flow and would predict $\omega_{\mathrm{tt}}^{\mathrm{QC}}/\dot{\gamma} = 1/2$, see equation (58).

8 Summary

We have studied the fluctuations and deformation of a 2d vesicle in shear flow at finite temperature. In the limit of small deformations from a circle, we have derived analytical Langevin-type equations of motion, which are nonlin-

ear due to the length constraint. A mean-field treatment allows approximate predictions for the stationary correlation functions and time autocorrelation functions of the deformation amplitudes, which agree quantitatively with simulation data. Deviations of the stationary correlations from the mean-field predictions in the lowest mode are explained quantitatively in a low-temperature expansion of the original constrained Langevin equations. The mean inclination angle and the tank-treading frequency are better described by a deterministic 2d Keller-Skalak theory. Fluctuations of the inclination angle are also determined quantitatively. Theory and simulations agree well for low excess lengths, but differ for larger excess lengths.

The good quantitative agreement of mesoscale simulations of vesicles in flow with detailed theoretical calculations demonstrates the predictive power of these simulation methods for more complex flow geometries.

Appendix A. Derivation of the equations of motion

We derive here in detail the deterministic equation of motion for the deformation amplitudes u_m in the quasi-circular limit as sketched in Section 3. Area conservation fixes u_0 in terms of the other u_m

$$u_0 = -\frac{1}{\sqrt{8\pi}} \sum_{m \neq 0} |u_m|^2. \tag{A.1}$$

The contour length L of the membrane is calculated to second order in u to be

$$L = 2\pi R_0 + \frac{R_0}{2} \sum_{m \neq 0} (m+1)(m-1)|u_m|^2, \tag{A.2}$$

thus giving the excess length Δ (18).

The local curvature k evaluates to

$$R_0 k(\phi) = 1 - u''(\phi) = 1 + \sum_{m \neq 0} m^2 u_m \frac{\exp(im\phi)}{\sqrt{2\pi}}. \tag{A.3}$$

This leads to the bending energy (ignoring constant terms)

$$\mathcal{H}_\kappa = \frac{\kappa}{4R_0} \sum_{m \neq 0} \left(m^2 - 1\right)\left(m^2 - 3/2\right)|u_m|^2. \tag{A.4}$$

The bending forces (8) are determined by the deformation amplitudes u_m and by the instantaneous tension

$$\Sigma(\phi) \equiv \frac{\kappa}{R_0}\left(\sigma + \sum_{m \neq 0} \sigma_m \frac{\exp(im\phi)}{\sqrt{2\pi}}\right). \tag{A.5}$$

The homogeneous tension $\kappa\sigma/R_0$ has been included into the energy (20).

We now calculate the flow field, which satisfies the force balance at the circular membrane and the boundary conditions. In polar coordinates, the general solution of Stokes' equation can be expanded into the fundamental modes [37]

$$
\begin{aligned}
\mathbf{v}_m^{\Phi,\pm} &\equiv \boldsymbol{\nabla}(r^{\pm|m|}\exp(im\phi))/\sqrt{2\pi}, \\
p_m^{\Phi,\pm} &\equiv 0, \\
\mathbf{v}_m^{P,\pm} &\equiv \frac{1}{2(1\pm|m|)\sqrt{2\pi}}\left(\frac{|m|\pm2}{2|m|}r^2\boldsymbol{\nabla}(r^{\pm|m|}\exp(im\phi))\right. \\
&\qquad \left. -\mathbf{r}r^{\pm|m|}\exp(im\phi)\right), \\
p_m^{P,\pm} &\equiv \eta_\alpha r^{\pm|m|}\exp(im\phi)/\sqrt{2\pi}.
\end{aligned}
\tag{A.6}
$$

In this representation the cases $|m|=1$ and $|m|=0$ are special and have to be treated separately. $\mathbf{v}_{\pm1}^{\Phi,\pm}$ and $\mathbf{v}_0^{\Phi,\pm}$ correspond to constant flow and rotational flow, respectively. $\mathbf{v}_{\pm1}^{P,\pm}$ is undefined and $\mathbf{v}_0^{P,\pm}$ corresponds to a fluid source at the origin, which does not exist in our setting. Therefore only one set of modes exists for these mode numbers, and not all boundary conditions can be fulfilled simultaneously. This is the mathematical manifestation of the Stokes paradox [37]. We therefore exclude the possibility of constant external flow. It follows from the boundary conditions that the induced velocity field on the inside must be composed of "+" modes, and of "−" modes on the outside.

The corresponding hydrodynamic stress tensor reads in (r,ϕ) components

$$
\begin{aligned}
\mathbf{T}_m^{\Phi,\pm} = {}& 2\eta r^{\pm|m|-2}\frac{\exp(im\phi)}{\sqrt{2\pi}} \\
&\times \begin{pmatrix} |m|(|m|\mp1) & im(\pm|m|-1) \\ im(\pm|m|-1) & -|m|(|m|\mp1) \end{pmatrix}
\end{aligned}
\tag{A.7}
$$

and

$$
\mathbf{T}_m^{P,\pm} = \eta r^{\pm|m|}\frac{\exp(im\phi)}{2\sqrt{2\pi}}\begin{pmatrix} \pm|m|-2 & im \\ im & \mp|m|-2 \end{pmatrix}.
\tag{A.8}
$$

We can now express the 2d Oseen tensor in spectral components. The radial and polar components of the fluid velocity and hydrodynamic force at the reference circle are expanded into Fourier modes analogous to the expansion (17). The velocity field at the reference sphere together with the boundary conditions uniquely determines the expansion (A.6). From the spatial velocity field the hydrodynamic force $\mathbf{f}^\pm \equiv \mathbf{T}^\pm \cdot \mathbf{n}$ can be calculated, leading to

$$
\begin{pmatrix} f_m^{r,\mathrm{ind}} \\ f_m^{\phi,\mathrm{ind}} \end{pmatrix} = \frac{\eta_\mathrm{in}+\eta_\mathrm{out}}{R_0}\begin{pmatrix} 2|m| & 2i\,\mathrm{sign}(m) \\ -2i\,\mathrm{sign}(m) & 2|m| \end{pmatrix}\cdot\begin{pmatrix} v_m^{r,\mathrm{ind}} \\ v_m^{\phi,\mathrm{ind}} \end{pmatrix}.
\tag{A.9}
$$

In the absence of the vesicle the applied external flow must be regular everywhere. Therefore apart from constant flow and constant rotation only the "+" modes contribute in the expansion (A.6). To avoid the intricacies of the Stokes paradox, we neglect the possibility of constant flow. A general expansion of the external flow therefore reads

$$
\mathbf{v}^\infty = \sum_m \Phi_m^\infty \mathbf{v}_m^{\Phi,+} + P_m^\infty \mathbf{v}_m^{P,+} + \Omega r\mathbf{e}_\phi.
\tag{A.10}
$$

The last term in this expansion corresponds to rotational flow with the vorticity Ω. For a finite viscosity contrast there is a jump in the traction

$$
\begin{aligned}
\begin{pmatrix} f^{r,\infty} \\ f^{\phi,\infty} \end{pmatrix} = {}& \sum_m \frac{\exp(im\phi)}{\sqrt{2\pi}}(\eta_\mathrm{in}-\eta_\mathrm{out}) \\
&\times \left[\begin{pmatrix} 2|m|(|m|-1) \\ 2im(|m|-1) \end{pmatrix}\Phi_m^\infty + \begin{pmatrix} |m|/2-1 \\ im/2 \end{pmatrix}P_m^\infty \right].
\end{aligned}
\tag{A.11}
$$

For the specific case of external linear shear flow

$$
\begin{aligned}
\mathbf{v}^\infty &= \dot\gamma y\mathbf{e}_x = (\dot\gamma/2)(y\mathbf{e}_x+x\mathbf{e}_y)-(\dot\gamma/2)(x\mathbf{e}_y-y\mathbf{e}_x) = \\
&\quad -(i\dot\gamma\sqrt{2\pi}/8)\left[\mathbf{v}_2^{\Phi,+}-\mathbf{v}_{-2}^{\Phi,+}\right]-(\dot\gamma/2)r\mathbf{e}_\phi,
\end{aligned}
\tag{A.12}
$$

we can read off the only non-vanishing components

$$
\begin{aligned}
\Phi_2^\infty &= -\Phi_{-2}^\infty = -i\sqrt{2\pi}\dot\gamma/8, \\
\Omega &= -\dot\gamma/2.
\end{aligned}
\tag{A.13}
$$

The flow at the vesicle membrane is subject to the incompressibility condition $D_t\sqrt{g} \equiv (\partial_t + \mathbf{v}\cdot\boldsymbol{\nabla})\sqrt{g}=0$, which can be cast in the equivalent form $\mathbf{t}\cdot\partial_\phi\mathbf{v}(\mathbf{r}(\phi))=0$. To leading order in the deformation, this condition reads

$$
v_r(R_0)+\partial_\phi v_\phi(R_0)=0.
\tag{A.14}
$$

Separating the induced flow from the external flow, we have in Fourier components

$$
\begin{aligned}
v_m^{r,\mathrm{ind}}(R_0)&+imv_m^{\phi,\mathrm{ind}}(R_0)=-v_m^{r,\infty}(R_0)-imv_m^{r,\infty}(R_0)= \\
&|m|(|m|-1)R_0^{|m|-1}\Phi_m^\infty+\frac{m^2}{4(|m|+1)}P_m^\infty.
\end{aligned}
\tag{A.15}
$$

Using this relation, we can eliminate v_m^ϕ and obtain

$$
\begin{aligned}
f_m^r = {}& 2\frac{\eta_\mathrm{out}}{R_0}(\lambda+1)\frac{m^2-1}{|m|}v_m^{r,\mathrm{ind}} \\
&+\Phi_m^\infty 2(|m|-1)\frac{\eta_\mathrm{out}}{R_0}\left[|m|(\lambda-1)+(\lambda+1)\right]+P_m^\infty.
\end{aligned}
\tag{A.16}
$$

Imposing the force balance (11) leads to

$$
v_m^{\mathrm{ind},r}=-(\kappa/\eta_\mathrm{out}R_0^2)\Gamma_m E_m(\sigma)u_m+B_m\Phi_m^\infty R_0,
\tag{A.17}
$$

with

$$
B_m \equiv -\frac{m^2(\lambda-1)+|m|(\lambda+1)}{(\lambda+1)(|m|+1)},
\tag{A.18}
$$

and where the mobility Γ_m is defined in equation (24). From the induced velocity, we obtain the radial component of the full velocity field

$$
v_m^r = v_m^{r,\mathrm{ind}}+v_m^{r,\infty}=v_m^{r,\mathrm{ind}}+|m|\Phi_m^\infty.
\tag{A.19}
$$

This leads directly to the advection equation (25).

References

1. M. Kraus, W. Wintz, U. Seifert, R. Lipowsky, Phys. Rev. Lett. **77**, 3685 (1996).
2. T. Biben, C. Misbah, Phys. Rev. E **67**, 031908 (2003).
3. J. Beaucourt, F. Rioual, T. Seon, T. Biben, C. Misbah, Phys. Rev. E **69**, 011906 (2004).
4. F. Rioual, T. Biben, C. Misbah, Phys. Rev. E **69**, 061914 (2004).
5. H. Noguchi, G. Gompper, Phys. Rev. Lett. **93**, 258102 (2004).
6. H. Noguchi, G. Gompper, Phys. Rev. E **72**, 011901 (2005).
7. P.M. Vlahovska, R.S. Gracia, Phys. Rev. E **75**, 16313 (2007).
8. K. de Haas, C. Blom, D. van den Ende, M.H.G. Duits, J. Mellema, Phys. Rev. E **56**, 7132 (1997).
9. V. Kantsler, V. Steinberg, Phys. Rev. Lett. **95**, 258101 (2005).
10. B. Lorz, R. Simson, J. Nardi, E. Sackmann, Europhys. Lett. **51**, 468 (2000).
11. M. Abkarian, C. Lartigue, A. Viallat, Phys. Rev. Lett. **88**, 068103 (2002).
12. U. Seifert, Phys. Rev. Lett. **83**, 876 (1999).
13. I. Cantat, C. Misbah, Phys. Rev. Lett. **83**, 880 (1999).
14. S. Sukumaran, U. Seifert, Phy. Rev. E **64**, 11916 (2001).
15. J. Beaucourt, T. Biben, C. Misbah, Europhys. Lett. **67**, 676 (2004).
16. V. Kantsler, V. Steinberg, Phys. Rev. Lett. **96**, 36001 (2006).
17. M. Mader, V. Vitkova, M. Abkarian, A. Viallat, T. Podgorski, Eur. Phys. J. E **19**, 389 (2006).
18. C. Misbah, Phys. Rev. Lett. **96**, 28104 (2006).
19. H. Noguchi, G. Gompper, Phys. Rev. Lett. **98**, 128103 (2007).
20. V. Lebedev, K.S. Turitsyn, S.S. Vergeles, Phys. Rev. Lett. **99**, 218101 (2007).
21. G. Danker, T. Biben, T. Podgorski, C. Verdier, C. Misbah, Phys. Rev. E **76**, 041905 (2007).
22. U. Seifert, Eur. Phys. J. B **8**, 405 (1999).
23. A. Malevanets, R. Kapral, J. Chem. Phys. **110**, 8605 (1999).
24. A. Malevanets, R. Kapral, J. Chem. Phys. **112**, 7260 (2000).
25. N. Kikuchi, C.M. Pooley, J.F. Ryder, J.M. Yeomans, J. Chem. Phys. **119**, 6388 (2003).
26. J.M. Yeomans, Physica A **369**, 159 (2006).
27. A. Lamura, G. Gompper, T. Ihle, D.M. Kroll, Europhys. Lett. **56**, 319 (2001).
28. A. Lamura, G. Gompper, Eur. Phys. J. E **9**, 477 (2002).
29. N. Kikuchi, J.F. Ryder, C.M. Pooley, J.M. Yeomans, Phys. Rev. E **71**, 061804 (2005).
30. M. Ripoll, R.G. Winkler, G. Gompper, Phys. Rev. Lett. **96**, 188302 (2006).
31. H. Noguchi, G. Gompper, Proc. Natl. Acad. Sci. U.S.A. **102**, 14159 (2005).
32. S.R. Keller, R. Skalak, J. Fluid. Mech. **120**, 27 (1982).
33. M. do Carmo, *Differential Geometry of Curves and Surfaces* (Prentice Hall, Englewood Cliffs, NJ, 1976).
34. W. Helfrich, Z. Naturf. C **28**, 693 (1973).
35. O. Kratky, G. Porod, Rec. Trav. Chim. **68**, 1106 (1949).
36. L.D. Landau, E.M. Lifshitz, *Fluid mechanics*, Vol. **6** (London, Pergamon Press, 1959).
37. J. Happel, H. Brenner, *Low Reynolds number hydrodynamics* (Martinus Nijhoff Publishers, 1983).
38. G.B. Jeffery, P. Roy. Soc. A **102**, 161 (1922).
39. M. Ripoll, K. Mussawisade, R.G. Winkler, G. Gompper, Europhys. Lett. **68**, 106 (2004).
40. T. Ihle, D.M. Kroll, Phys. Rev. E **63**, 020201(R) (2001).
41. T. Ihle, E. Tüzel, D.M. Kroll, Phys. Rev. E **70**, 035701(R) (2004).
42. G. Gompper, D.M. Kroll, in *Statistical Mechanics of Membranes and Surfaces*, edited by D. Nelson, T. Piran, S. Weinberg, 2nd edition (World Scientific Publishing, Singapore, 2004) p. 390, chapt. 12.